Operando Microscopy Diagnosis of the Onset of Lithium

Plating in Transparent Lithium-ion Full Cells

Bingyuan Ma¹, Shubham Agrawal¹, Rajeev Gopal¹ and Peng Bai^{1,2,*}

¹ Department of Energy, Environmental & Chemical Engineering, Washington University in St. Louis,

St. Louis, MO 63130, United States of America

² Institute of Materials Science and Engineering, Washington University in St. Louis, St. Louis, MO

63130, United States of America

*Correspondence to: <u>pbai@wustl.edu</u>

Keywords: Fast charging, operando visualization, Li plating, three-electrode coin cell, differential

voltage

Abstract: The fast-charging capability is critical for the wide adoption of electric vehicles (EV), which,

however, can result in Lithium (Li) plating on the graphite anode that aggravates the cell degradation

and increases the safety risk. Li plating is also prone to occur during charging at low temperatures. In

this work, we fabricate Li-ion full cells in transparent glass capillaries to probe the real-time dynamic

evolution of the lithiated phases throughout the graphite anode toward the onset of lithium plating

during fast charging and under low temperatures. We observed that Li plating can occur well before

70% state of charge (SOC), even at a low C-rate and at room temperature. Our operando experiments

provide the direct proof that subtle features in the electrochemical responses are caused by the Li plating,

which can be utilized to improve battery management strategy. Mathematical simulations confirm that

the local overpotential due to the strong concentration polarization is the root cause of the axial reaction

heterogeneity in the graphite anode and the Li plating on the fully lithiated particles.

1. Introduction

Lithium-ion batteries (LIBs) have enabled successful electric vehicles (EVs).^{1,2} However, the wide adoption of EVs is still limited by the range anxiety and the re-charging time which is much longer than the re-fueling time of the internal combustion engine (ICE) vehicles.^{3,4} The key issue that limits the fast charging of LIBs, among other less severe degradation mechanisms, is the lithium (Li) plating on the graphite anode, compromising their cycle life and safety.⁵ During Li plating, the metal deposits do not form a smooth layer, but tend to grow whiskers and dendrites with high surface area to form an irreversible solid electrolyte interphase (SEI) layer that can exacerbate the nonuniform growths.⁶ The metal growths can penetrate the porous separator and short-circuit the cell, leading to fires and explosions. Therefore, it is crucial to develop the accurate yet predictive understanding of the onset of the Li plating on the anode during fast charging and/or under low temperatures.

While Li plating in LIBs has been detected using analytical methods such as differential voltage analysis, 7-11 and the high precision coulometry, 12 the diagnoses were usually postmortem, after plating a significant amount of Li. The real-time voltage characteristics were also linked to the onset of Li plating but are limited to half-cells which cannot be utilized for the full cell management. 10,13-16 Full cell incremental capacity analysis has long been used for cell degradation or even Li plating diagnosis. 17-19 The correlation between the characteristic peaks and the internal physical processes is yet to be verified by *operando* observations, which is necessary for investigating the dynamic evolution in graphite during the fast and understanding the onset of Li plating. Sophisticated *operando* techniques such as X-ray diffraction or tomography, 20-23 electron magnetic resonance, 24 neutron diffraction 25,26, and Raman spectroscopy 27,28 can probe the Li plating dynamics during the fast charging and are promising for deconvolution of the full cell signals. However, their spatiotemporal resolution is limited, which makes them hard to capture the rapid cell and electrochemical dynamics during a fast charging. 10 The optical microscope fulfills this requirement with micron-level resolution and fast imaging speed, 10,12,14,16,29-32 but requires careful cell design to be constructed in a sandwich configuration.

Here, we proved via operando experiments the causal relationship between the signature peaks in the

differential capacity/voltage curves and the onset of Li plating. The special capillary full cells were taken as the model system for the practical LIB sandwich cells to probe the dynamic evolution in graphite anodes during the fast-charging process. We first observed state of charge (SoC) heterogeneities along the axial direction for current densities higher than 2 mA cm⁻², which renders the current density a more appropriate parameter over C-rate for the cross-system comparison and evaluation. We then identified a clear voltage signature indicating the onset of Li plating on graphite anode with both phase-separating and solid-solution cathode materials, as proved by the visual observations. The larger format coin cells also showed similar voltage characteristics, with detailed evaluation using the differential capacitance analysis. Mathematical simulations reveal that both the axial SoC heterogeneity and the Li plating are caused by the strong polarization of the concentration overpotential along the axis, which becomes more significant at low temperature.

2. Results

2.1 SoC heterogeneity in graphite anode

We fabricated typical sandwich-structure full cells in glass capillaries $^{33-37}$ (Fig.1a) for the *operando* visualization with graphite as the anode and lithium iron phosphate (LFP) or lithium nickel manganese cobalt oxide (NMC811) as the cathode. The capillary full cell configuration allowed an accurate determination of current densities while monitoring the dynamic phase transformation in the entire graphite electrode. We employed high loadings of around 17 mg cm⁻² to achieve an electrode thickness of around 380 μ m.

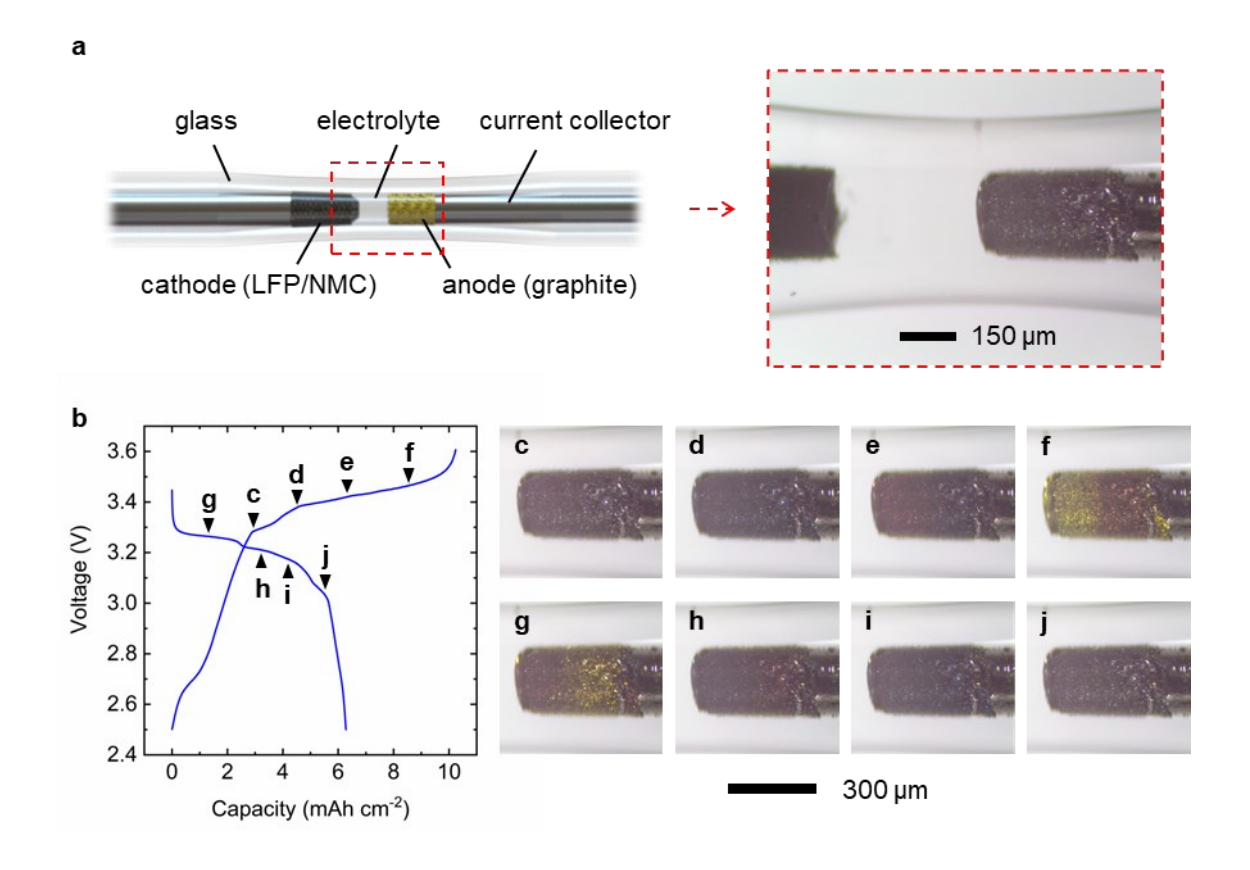


Figure 1. Axial heterogeneity in graphite during Li-ion intercalation and deintercalation. (a) The structure of the Li-ion capillary full cell. (b-j) Snapshots and the voltage response of the LFP|graphite full cell during the formation cycle at 0.5 mA cm⁻².

Figures 1b-j and Video S1 show the axial heterogeneity during the low-current formation cycle at 0.5

mA cm⁻² of an LFP|graphite capillary full cell. Graphite is known to exhibit several different colors as the SoC increases to form different phases or stages.³¹ During the charging process of the full cell, graphite particles remained grey until the voltage reaches the little plateau at around 3.3 V (Figs. 1b and 1c). A considerable capacity was consumed for the formation of the SEI at this point. The graphite particles changed color to blue (stage 3) homogeneously upon initial Li-ion intercalation via a solidsolution mechanism. This concurrent particle activation confirmed a uniform electronic conductivity of the electrode and mild concentration polarization in the electrolyte at low galvanostatic conditions. Once the entire graphite anode reached stage 3 (Fig. 1d), further Li-ion intercalation induced the transformation from stage 3 (blue) to stage 2 (red) via phase separation mechanism. 38,39 The red color (stage 2) originated from the front face of the electrode (facing the bulk electrolyte) and moved towards the back face (current collector) (Fig. 1e) due to an increasing concentration overpotential from front to back. The next phase transformation from red to gold (stage 1) followed a similar behavior until the graphite was fully lithiated (Fig. 1f). The phase transformations in the graphite were reversed during cell discharge. The gold to red and red to blue transformations also propagated from the front face to the back face of the electrode during delithiation, followed by a homogeneous color change to grey (Figs. 1g-j). Both the charging and discharging voltage responses as well as phase transformation mechanisms agreed well with the practical LFP|graphite full cells.⁴⁰ The observed phenomena are consistent with previous reports, 10,30 but the sandwich configuration within an ideal cylindrical geometry allows for a more accurate and practice-relevant determination of the current density and ionic flux to enable rigorous analysis.

2.2 Subtle voltage changes at the onset of Li plating

After the formation cycle, we performed galvanostatic charging on the capillary full cells at high current densities ranging from 2 to 6 mA cm⁻². However, even at 2 mA cm⁻², only the particles within ~100 µm from the front face became blue (Fig. 2 and Video S2). The phase transformation never reached the back face of the electrode as we had observed in the low-current case. The red and gold colors then appeared in sequence from the front face and the phase boundaries propagated concurrently toward the back face but never reached the current collector. The coexistence of all three different

lithiated stages indicated a strong variation of the overpotential along the axis. The Li plating started at the front face before the back face of the graphite electrode was lithiated. Interestingly, at the onset of Li plating, a little hump in the voltage response was observed as shown in Fig. 2a. Since LFP is a typical phase-separation material with a stable and flat voltage plateau, any voltage fluctuations in the full cell voltage profile should come from the anode. Therefore, the voltage hump must have been induced by the Li nucleation barrier on the fully lithiated graphite surface. 14 Replacing the LFP with the solidsolution cathode material, NMC811, did not affect the intercalation behavior of the graphite during fast charging (Figs. 2f-j). Despite the slanted full-cell voltage curve due to the NMC811 cathode, the onset of Li plating on graphite still showed a distinguishable voltage step as labeled in Fig. 2f. Figures 2k-o and Figs. 2p-t show the voltage profiles and the snapshots at the onset of Li plating in the operando experiments at the current densities ranging from 2 to 6 mA cm⁻² with LFP and NMC811 as cathodes, respectively. Similar voltage artifacts for Li plating, i.e. the hump with LFP as the cathode and the step with NMC811 as the cathode, were clearly identifiable in each case. The critical time of the onset of Li plating and the anode filling thickness both decreased with increasing the charging current densities during fast charging. We also discovered that the Li plating could begin well below the cutoff voltage since the Li plating can happen at low SoC. Both cathode and anode overpotential at the onset of Li plating increases at higher current densities but the equilibrium voltage is low for cathodes without a stable voltage plateau such as NMC at lower SoC. Therefore, in LFP|graphite cases where the cathode has a stable voltage plateau, the voltage magnitude of Li plating increases with the current density but it is the opposite in NMC|graphtie cases.

In fast-charging experiments, C-rate, which is scaled to the full capacity of the electrode, is commonly used to indicate the intensity of the applied current. However, for fair cross-system comparisons, the current density is physically more appropriate. Due to the high loadings of our electrodes, the C-rates converted from the high current densities appear low, from 0.32 C to 1.83 C. Li plating can occur before reaching 70% SoC (Figs. 2k-t).

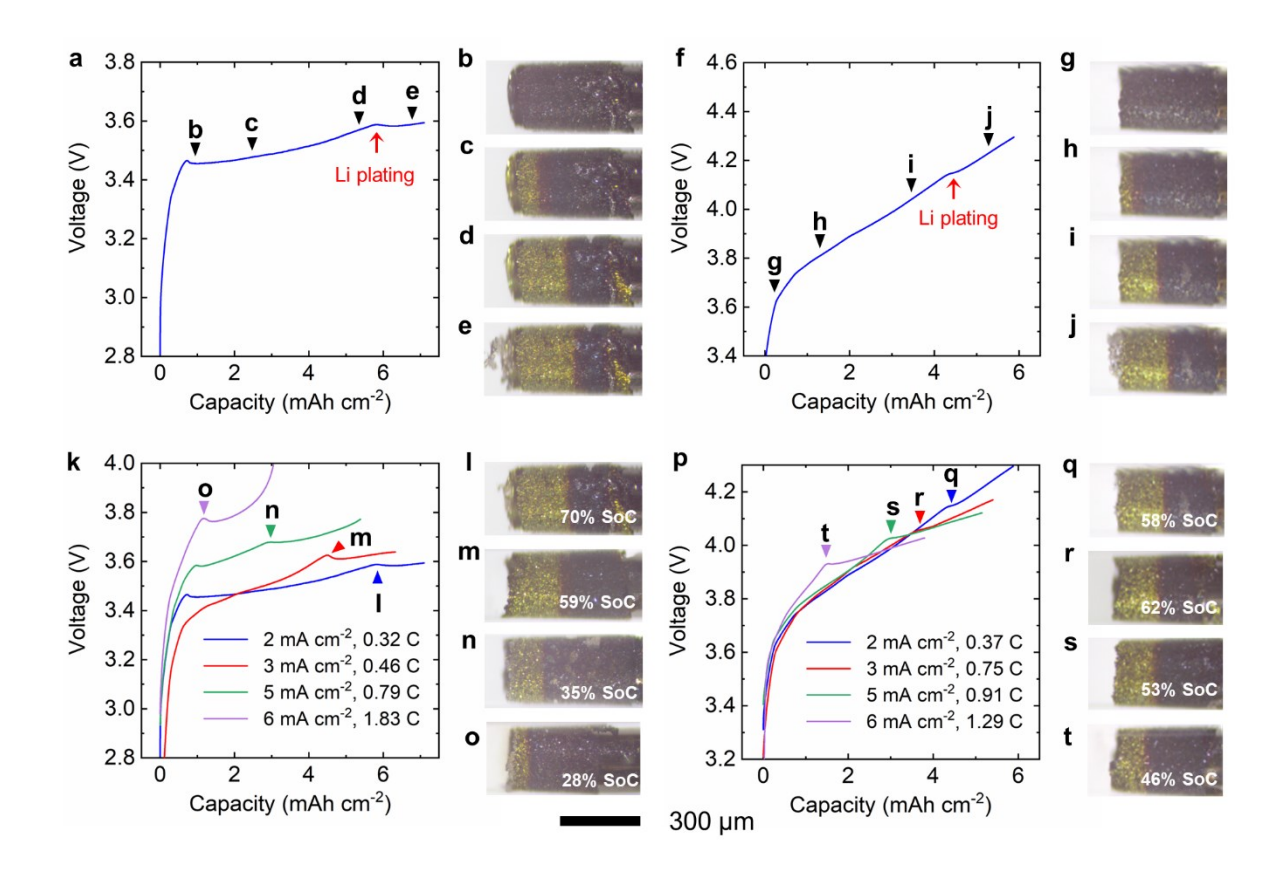


Figure 2. Operando diagnosis of the graphite anode during fast charging. (a-j) Voltage responses and the *operando* snapshots of the graphite during the fast charging at 2 mA cm⁻² with LFP (a-e) or NMC (f-j) cathode. (k-t) Voltage responses and the snapshots at the point of Li plating on the graphite during the fast charging at various current densities with LFP (k-o) or NMC (p-t) cathode. The C-rate at each current density is calculated based on the discharge capacity of the 0.5 mA cm⁻² formation cycle. Since the fast charging is performed at the second cycle where the charges can still be consumed for the interphases, the SoC of the onset of Li plating is estimated based on the *operando* images and the SoC of each phase.

The interplay between transport in solid and liquid phases governs both the charge heterogeneities and the Li plating during the fast charging process. 14,31,33 Since the characteristic diffusion time constant for graphite was $\tau_D = \frac{R^2}{D} \approx 20$ s, where R is around 4 µm (average particle radius) and D is 9×10^{-9} cm² s⁻¹, 31,41 the lithiation process prior to the onset of Li plating was not limited by solid-state diffusion. However, at high lithiation current densities, the concentration depletion in the electrolyte due to

diffusion in the electrolyte through the porous electrode can intensify the concentration overpotential variation along the thickness that promotes the strong axial charge heterogeneities.

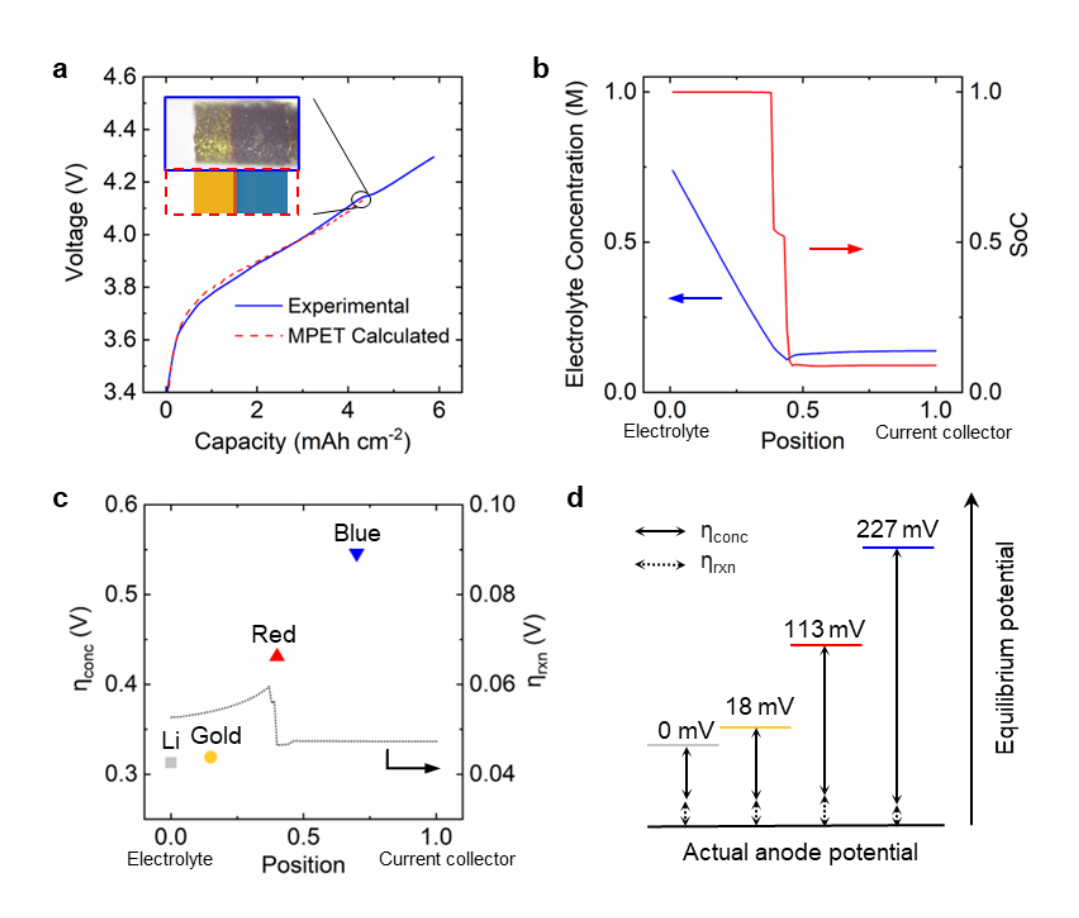


Figure 3. Mechanism of the Li plating during fast charging processes. (a) Experimental and MPET calculated voltage curve for the case of 2 mA cm⁻² with NMC as the cathode. The insets are the screenshot and the simulated graphite lithiation state at the point when Li plating starts. (b) The calculated electrolyte concentration and the solid state SoC along the anode thickness at the time frame when Li plating happens. (c) The calculated concentration overpotential and the reaction overpotential distribution along the anode thickness. (d) Schematic explanation of the mechanism of the Li plating and the graphite axial heterogeneity. The strong concentration overpotential gradient can lead to different equilibrium phases along the thickness at a certain anode potential. The Li plating starts when the equilibrium potential at the front face goes below 0 V.

To better understand this mechanism, we simulated the intercalation process during the fast charging

of the NMC811|Graphite capillary cell at 2 mA cm⁻² using the Multiphase Porous Electrode Theory (MPET) package. 42 We validated the simulation by comparing the voltage profile and the Li filling profile with the operando experimental results (Figs. 3a,b and Video S3). We selected the frame when the Li plating started to analyze the coexistence of four phases (blue, red, gold, and Li metal). The simulation showed the strongest electrolyte concentration depletion at the phase boundaries in the graphite anode (Fig. 3b) with the concentration at the electrode front face approaching the bulk concentration. To better understand the polarization, we estimated the concentration overpotential η_{conc} distribution in the porous electrode at the critical frame (Fig. 3c) by $V = \Delta U^{\theta} + \eta_{rxn} + \eta_{conc}$, where V is the cell voltage, ΔU^{θ} is the equilibrium potential difference between the cathode and anode for the corresponding lithiated graphite stages, and η_{rxn} is the reaction overpotential of the two electrodes estimated by the modified Bulter-Volmer equation.³⁹ Note that the concentration overpotential η_{conc} obtained from the simulation is induced by the strong concentration polarization determined by the transport equation, which also includes the ohmic contribution, only that the ohmic overpotential η_{ohm} can no longer be properly defined due to the concentration gradient and therefore the varying conductivity.⁴³ Our simulation confirmed the strongly varying concentration overpotential along the thickness of the graphite, which is responsible for the SoC heterogeneities and finally the Li plating. While the exchange current density is a function of both the electrolyte concentration and the SoC, the variations of the reaction overpotential for different parts (stages) of the electrode are negligible, compared with the concentration overpotentials (Fig. 3c). As explained schematically in Fig. 3d, at a certain anode potential, the equilibrium phases will be different along the thickness due to the strong concentration overpotential gradient. During fast charging, the anode potential keeps decreasing with increasing filling fractions and the phase boundaries moving towards higher concentration overpotential regions. The Li plating will start when the anode potential becomes low enough such that the equilibrium electrochemical potential at the front face drops below the Li reduction potential.

2.3 Voltage features of Li plating in practical cells

While the subtle voltage features of Li plating can be clearly captured in capillary full cells, a higher electrode area in the large format LIBs may conceal such artifacts. To validate our discoveries, we constructed three-electrode coin cells to test fast charging operations. We maintained an N/P ratio of around 0.8 in both NMC811|Graphite and LFP|Graphite systems to ensure Li plating on the anode.⁴⁴ We used the same current densities in the coin-cell systems as the capillary cells for the fair cross-system validation and monitored the anode vs. reference (Li metal) and the cathode vs. anode voltages simultaneously yet independently.

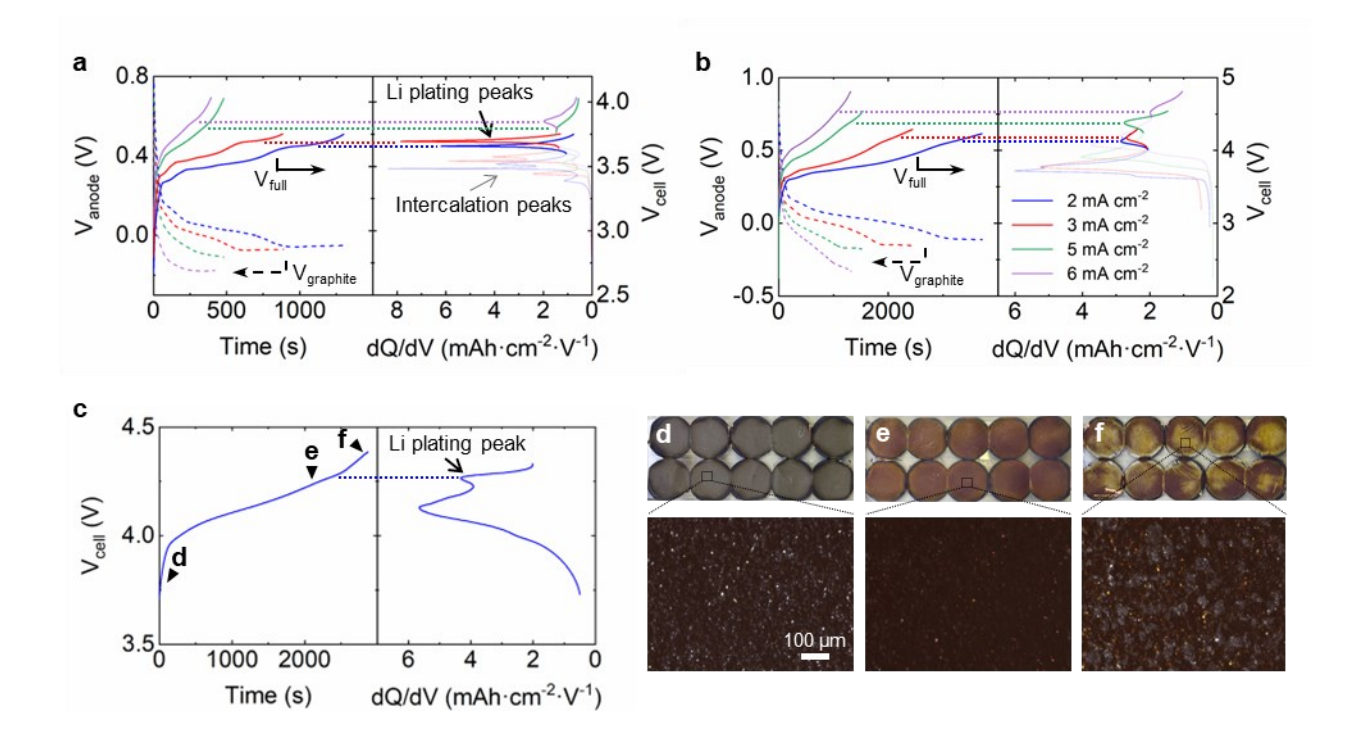


Figure 4. Li plating analysis during fast charging in 3-electrode coin cells and the commercial coin cell. (a,b) The full cell and graphite voltage responses and the corresponding full cell dQ/dV results in (a) LFP|Graphite, and (b) NMC|Graphite coin cells. The solid lines belong to the full cell and the dashed lines are the graphite voltage. The dQ/dV plots are plotted by taking the full cell voltage as the y-axis for a better comparison with the voltage curve. The Li plating peaks in the full cell dQ/dV plot are represented as thick solid lines. (c) The voltage response and the dQ/dV analysis of the commercial 45 mAh NMC coin cell being charged at 1C (~2 mA cm⁻²). (d-f) The ex-situ images taken at different SoCs during the 1C charging.

As shown in Figs. 4a and 4b, the anticipated Li plating humps or steps cannot be clearly identified in

the terminal voltage curves of the full cells especially at high current densities, but voltage plateaus were clearly revealed in the anode vs. reference voltage profiles. These independently measured anode plateaus appear to be the reason for the Li plating peaks identified in the differential capacitance curves.

It is noteworthy that the Li plating did not necessarily occur as soon as the measured graphite potential dropped below zero. While the three-electrode system effectively rules out the voltage uncertainties due to ion polarization at the counter electrode, the anode reaction overpotential and the uncompensated IR drop can still be significant during high-rate lithiation. Although the voltage artifact of Li plating became less clear at higher current densities, i.e. 5 and 6 mA cm⁻², a rigorous dQ/dV analysis could reveal corresponding peaks due to the existence of the Li plating plateaus in the anode voltage curves, as shown in Figs. 4a and 4b.

Similar signature of Li plating was also found in the fast charging process of the high-loading (45 mAh) commercial coin cells. At 1C rate (~2 mA cm⁻²), the Li plating peak appears at 4.27 V in the differential capacitance analysis (Fig. 4c), lower than a practical 4.3 V cutoff.⁴⁵ Instead of overcharging the cell, the Li plating starts at only around 60 % SoC at this charging rate. The Li plating was further confirmed by taking the ex-situ images after opening the cells at different SoCs (Figs. 4d-f). The Li plating on top of gold particles was clearly captured in the microscopic image after passing the Li plating peak, consistent with our *operando* diagnosis results. It is important to mention that the Li plating was also found near the edge of the electrode where the graphite particles remain grey. This part of the Li could still originate from the nearby gold particles but preferentially grow towards the edge where the stacking pressure is lower due to the anode overhang.

2.4 Fast charging diagnosis under low temperature

Li plating is intensified in low-temperature conditions, regardless of the charging C rates. 8,15,16 To understand the onset of Li plating at low temperature, we repeated the *operando* diagnosis at -20 °C with NMC811|Graphite capillary full cells. We switched to a low-temperature-compatible electrolyte 1 M LiPF₆ in EC/PC/EMC (1:1:8 by weight) to maintain sufficient ionic conductivity. 46

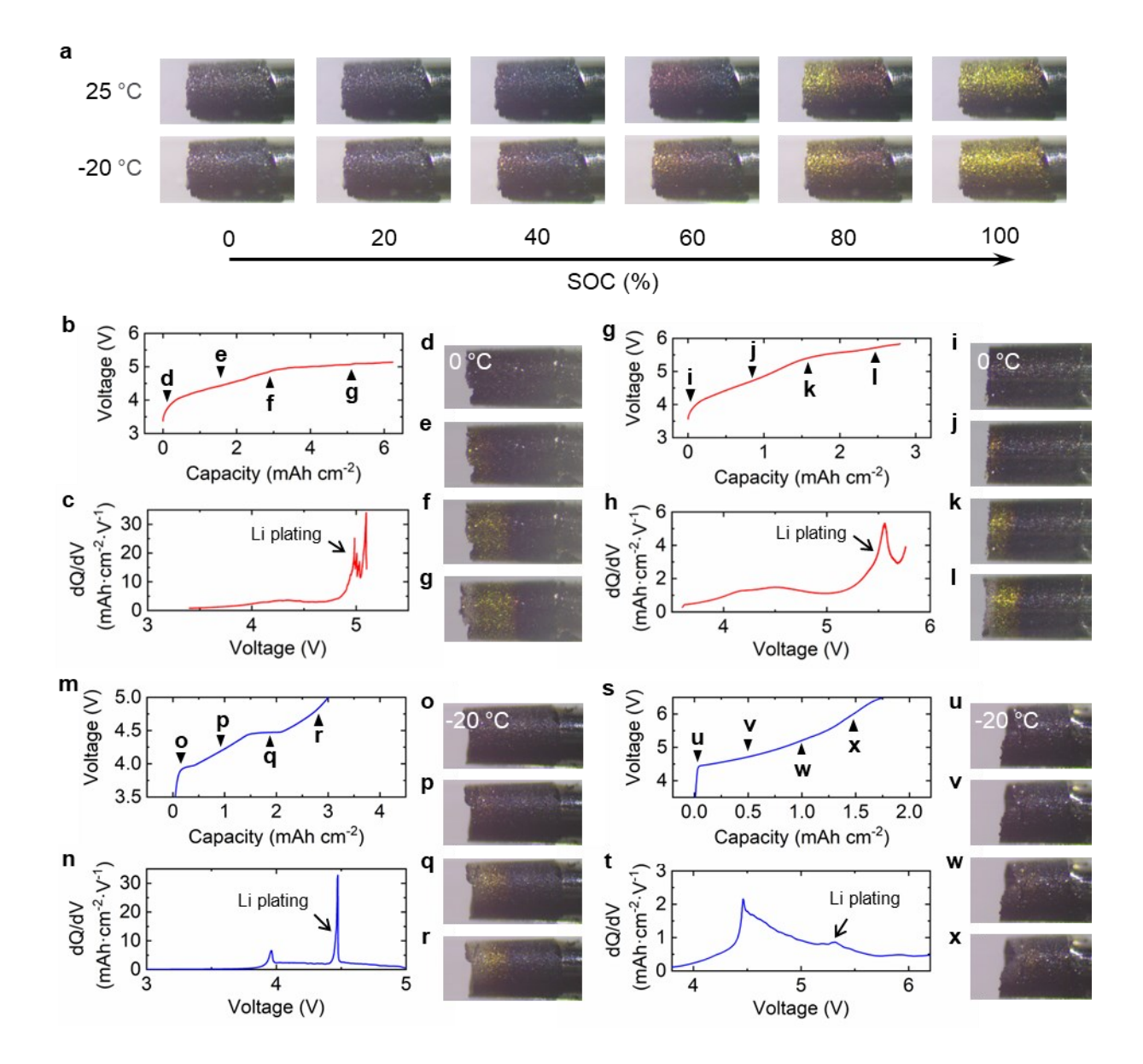


Figure 5. Fast charging *operando* diagnosis at different temperatures. (a) The low-rate lithiation behavior comparison at 0.5 mA cm⁻² between the low temperature and the room temperature. (b-l) Voltage, differential capacity analysis, and screenshots at 0 °C and the charging rate of 2 mA cm⁻² (b-g) and 6 mA cm⁻² (g-l). (m-x) Voltage, differential capacity analysis, and screenshots at -20 °C and the charging rate of 2 mA cm⁻² (m-r) and 6 mA cm⁻² (s-x).

The low-rate lithiation at 0.5 mA cm⁻² at low temperature exhibited stronger axial heterogeneities than at room temperature, as indicated by the co-existence of the three phases along the axis at the 40% and 60% SoCs (Fig. 5a and Video S4). This difference is attributable to the reduced ionic conductivity

and Li⁺ diffusivity at the low temperatures, which lead to stronger concentration overpotential gradients along the axial direction. The stronger concentration overpotential gradients can lead to earlier Li plating during fast charging at low temperatures than at room temperature. To test this, the fast charging experiment was performed at 0 °C (Figs. 5b-l and Videos S5 and S6) and -20 °C (Figs. 5m-x and Videos S7 and S8). At 2 mA cm⁻², the critical Li plating capacity was 4.2 mAh cm⁻² at room temperature but decreases to 3.5 mAh cm⁻² at 0 °C and 1.5 mAh cm⁻² at -20 °C (Figs. 5b-g and 5m-r), which is consistent with the prediction. At 6 mA cm⁻², the voltage artifact for Li plating was harder to notice directly from the voltage response, especially at -20 °C, but still traceable from the differential capacity analysis (Figs. 5g-k and 5s-x). However, such a small signature could easily diminish in the practical large-format cells, which makes the differential capacity analysis incapable of alarming the Li plating at low temperatures and high current densities. The higher Li-plating critical voltage at 0 °C than at -20 °C is due to the higher N/P ratio. Interestingly, the plated Li at low temperatures exhibited a more uniform mossy Li growths, covering the entire front face, rather than forming localized Li whiskers in the cases at room temperature (Fig. 2).

3. Conclusion

In this work, we performed *operando* diagnosis of the graphite anode during the fast charging process in our special capillary full cells. At high charging current densities (2-6 mA cm⁻²), but equivalently low C-rates (0.32 to 1.83 C due to the electrode loading), the graphite shows strong SoC heterogeneity along the electrode thickness. Such SoC heterogeneity, i.e., the coexistence of all three different lithiated stages, is absent at 0.5 mA cm⁻². Li plating is observed before the graphite electrode is lithiated to 70% SoC even at 0.32 C, which emphasizes that the current density is more accurate than C-rate to describe the charging rate under such a strong axial heterogeneity. Subtle full-cell voltage features were captured at the onset of Li plating, either a hump when using the phase-separating material as the cathode or a step when using the solid-solution material as the cathode. Similar voltage features were also detected in the practical coin cells and were more obvious in the voltage differential analysis. MPET simulations

reveal a strong concentration overpotential gradient along the axis of the anode during fast charging which can lead to the axial SoC heterogeneity and the Li plating. The gradient of the concentration overpotential can become more significant at low temperature due to the reduced diffusivity and causes stronger heterogeneity and earlier Li plating. Our work offers a useful method for developing fast-charging protocol for a given cell configuration, or determining the critical loading based on the required charging rates and working temperatures.

4. Experimental Section

Materials: Dimethyl carbonate (DMC, anhydrous, ≥99%), ethylene carbonate (EC, anhydrous, 99%), propylene carbonate (PC, anhydrous, 99.7%), ethyl methyl carbonate (EMC, 99%), Lithium hexafluorophosphate (LiPF₆, battery grade, ≥99.99% trace metals basis), 1 M LiPF₆ solution in EC/DMC = 50/50 (v/v) were purchased from Sigma-Aldrich. All the solvents were dried using molecular sieves for at least 3 days before use. The salt was dried at 100 °C for 48 hours before use. 0.01-inch diameter stainless steel wires were purchased from McMaster-Carr. 5 μL glass capillaries are purchased from VWR. Polypropylene-Polyethylene-Polypropylene (PP-PE-PP) tri-layer battery separator (Celgard 2325, 25 μm thickness), copper foil for battery anode substrate (9 μm thickness), aluminum foil for battery cathode substrate (15 μm thickness), conductive acetylene black, HSV900 PVDF binder was purchased from MTI Corporation. 45 mAh EEMB coin cells were purchased from Amazon.

Electrode preparation: Graphite/LFP/NMC811, conductive acetylene black and PVDF binder were thoroughly mixed into slurry with NMP at a weight ratio of 8.5:0.5:1 (for graphite) and 8:1:1 (for cathodes). The slurry was cast onto the copper (graphite) or aluminum (cathodes) foil and dried at 120 °C overnight before cutting into disk electrodes. For the 3-electrode coin cells, the graphite mass loading is around 3.5 mg cm⁻². The N/P ratio is around 0.8 to ensure the Li plating.

Cells fabrication and electrochemical testing: All cells were assembled in an Ar-filled glove box with

H₂O and O₂ concentration < 0.5 ppm. For the capillary full cells, the two electrode slurry was first filled in the glass capillary with the graphite loading of around 5-6 mAh cm⁻² and the N/P ratio of around 0.9, then dried at 60 °C overnight in atmosphere followed by a 10-hour vacuum drying at 120 °C. The glass capillaries were pulled 0.5 mm longer between the two electrodes with a vertical type micropipette puller (PC-10, Narishige Co., Ltd). The pulled capillary was fixed onto a piece of glass slide using epoxy. Electrolytes were filled in the capillary by a syringe. Two electrodes were then fixed at the pulled part by the stainless steel wires. For the 3-electrode coin cells, an additional copper wire was placed between two trilayer separators with a small piece of Li as the reference electrode. *Operando* images were captured by an optical microscope (MU500, AmScope). Electrochemical tests were conducted with a Gamry potentiostat (Reference 600+, Gamry Instruments), an Arbin battery tester (LBT 20084, Arbin Instruments) and a Land battery testing system (CT3001A, Lanhe instruments).

MPET simulation: The Multiphase Porous Electrode Theory (MPET) which is an open-source Python code developed by Bazant and coworkers, ⁴² has been used for the simulations. The theory uses bilayer regular solution model with gradient penalty to calculate the chemical potential of graphite. ³⁸ The chemical potential of NMC811 is fitted from low current half-cell experiments. ⁴⁷ The thicknesses and porosities of electrodes were consistent with the experimental setup. Since the model requires C-rate as the driving condition, we used the derived C-rate from the current density of 2 mA cm⁻². The electrolyte is modeled using dilute electrolyte model. We used the reaction parameters shown in Table 1 to simulate the solid-phase dynamics.

Table 1. MPET simulation parameters

Parameter	Graphite	NMC811
Diffusion coefficient, D	$9 \times 10^{-13} \text{ m}^2 \text{ s}^{-1}$	$5 \times 10^{-13} \text{ m}^2 \text{ s}^{-1}$
Exchange current density, j ₀	83 A m ²	0.5 A m ²
Gradient penalty coefficient, κ	$5.0148 \times 10^{-10} \text{ J m}^{-1}$	$5.0148 \times 10^{-10} \text{ J m}^{-1}$
Electrode thickness	0.000385 m	0.000356 m
Porosity	0.4	0.5

Supporting information

Supporting information is available online.

Video S1: Operando diagnosis of the graphite anode during 0.5 mA cm⁻² formation cycle.

Video S2: *Operando* diagnosis of the graphite anode during 2 mA cm⁻² fast charging with LFP as the cathode.

Video S3: *Operando* diagnosis of the graphite anode during 2 mA cm⁻² fast charging with NMC as the cathode.

Video S4: Comparison of the graphite intercalation dynamics between room and low temperatures.

Video S5: *Operando* diagnosis of the graphite anode during 2 mA cm $^{-2}$ fast charging with NMC as the cathode at 0 °C.

Video S6: *Operando* diagnosis of the graphite anode during 6 mA cm $^{-2}$ fast charging with NMC as the cathode at 0 °C.

Video S7: *Operando* diagnosis of the graphite anode during 2 mA cm $^{-2}$ fast charging with NMC as the cathode at -20 °C.

Video S8: *Operando* diagnosis of the graphite anode during 6 mA cm $^{-2}$ fast charging with NMC as the cathode at -20 °C.

Acknowledgments

This work is supported by two National Science Foundation grants (Award No. 1934122 and 2044932).

P.B. acknowledges the faculty startup support from Washington University in St. Louis.

Competing interests

The authors declare no competing financial interests.

References

- (1) Lu, J.; Chen, Z.; Pan, F.; Curtiss, L. A.; Amine, K. The Role of Nanotechnology in the Development of Battery Materials for Electric Vehicles. *Nat Nanotechnol* **2016**, *11* (12), 1031–1038. https://doi.org/10.1038/nnano.2010.207.
- (2) Mahmoudzadeh Andwari, A.; Pesiridis, A.; Rajoo, S.; Martinez-Botas, R.; Esfahanian, V. A Review of Battery Electric Vehicle Technology and Readiness Levels. *Renewable and Sustainable Energy Reviews* **2017**, 78 (March), 414–430. https://doi.org/10.1016/j.rser.2017.03.138.
- (3) Tomaszewska, A.; Chu, Z.; Feng, X.; O'Kane, S.; Liu, X.; Chen, J.; Ji, C.; Endler, E.; Li, R.; Liu, L.; Li, Y.; Zheng, S.; Vetterlein, S.; Gao, M.; Du, J.; Parkes, M.; Ouyang, M.; Marinescu, M.; Offer, G.; Wu, B. Lithium-Ion Battery Fast Charging: A Review. *eTransportation* **2019**, *I*, 100011. https://doi.org/10.1016/j.etran.2019.100011.
- (4) Weiss, M.; Ruess, R.; Kasnatscheew, J.; Levartovsky, Y.; Levy, N. R.; Minnmann, P.; Stolz, L.; Waldmann, T.; Wohlfahrt-Mehrens, M.; Aurbach, D.; Winter, M.; Ein-Eli, Y.; Janek, J. Fast Charging of Lithium-Ion Batteries: A Review of Materials Aspects. *Adv Energy Mater* **2021**, *11* (33). https://doi.org/10.1002/aenm.202101126.
- (5) Goodenough, J. B.; Kim, Y. Challenges for Rechargeable Li Batteries. *Chemistry of Materials* **2010**, *22* (3), 587–603. https://doi.org/10.1021/cm901452z.
- (6) Peled, E. The Electrochemical Behavior of Alkali and Alkaline Earth Metals in Nonaqueous Battery Systems—The Solid Electrolyte Interphase Model. *J Electrochem Soc* **1979**, *126* (12), 2047–2051. https://doi.org/10.1149/1.2129891.
- (7) Campbell, I. D.; Marzook, M.; Marinescu, M.; Offer, G. J. How Observable Is Lithium Plating? Differential Voltage Analysis to Identify and Quantify Lithium Plating Following Fast Charging of Cold Lithium-Ion Batteries. *J Electrochem Soc* **2019**, *166* (4), A725–A739. https://doi.org/10.1149/2.0821904jes.
- (8) Petzl, M.; Danzer, M. A. Nondestructive Detection, Characterization, and Quantification of Lithium Plating in Commercial Lithium-Ion Batteries. *J Power Sources* **2014**, *254*, 80–87. https://doi.org/10.1016/j.jpowsour.2013.12.060.
- (9) O'Kane, S. E. J.; Campbell, I. D.; Marzook, M. W. J.; Offer, G. J.; Marinescu, M. Physical Origin of the Differential Voltage Minimum Associated with Lithium Plating in Li-Ion Batteries. *J Electrochem Soc* **2020**, *167* (9), 090540. https://doi.org/10.1149/1945-7111/ab90ac.
- (10) Chen, Y.; Chen, K. H.; Sanchez, A. J.; Kazyak, E.; Goel, V.; Gorlin, Y.; Christensen, J.; Thornton, K.; Dasgupta, N. P. Operando Video Microscopy of Li Plating and Re-Intercalation on Graphite Anodes during Fast Charging. *J Mater Chem A Mater* **2021**, *9* (41), 23522–23536. https://doi.org/10.1039/d1ta06023f.
- (11) Yang, X. G.; Ge, S.; Liu, T.; Leng, Y.; Wang, C. Y. A Look into the Voltage Plateau Signal for Detection and Quantification of Lithium Plating in Lithium-Ion Cells. *J Power Sources* **2018**, 395 (May), 251–261. https://doi.org/10.1016/j.jpowsour.2018.05.073.
- (12) Burns, J. C.; Stevens, D. A.; Dahn, J. R. In-Situ Detection of Lithium Plating Using High Precision Coulometry. *J Electrochem Soc* **2015**, *162* (6), A959–A964.

- https://doi.org/10.1149/2.0621506jes.
- (13) Uhlmann, C.; Illig, J.; Ender, M.; Schuster, R.; Ivers-Tiffée, E. In Situ Detection of Lithium Metal Plating on Graphite in Experimental Cells. *J Power Sources* **2015**, *279*, 428–438. https://doi.org/10.1016/j.jpowsour.2015.01.046.
- (14) Gao, T.; Han, Y.; Fraggedakis, D.; Das, S.; Zhou, T.; Yeh, C. N.; Xu, S.; Chueh, W. C.; Li, J.; Bazant, M. Z. Interplay of Lithium Intercalation and Plating on a Single Graphite Particle. *Joule* **2021**, *5* (2), 393–414. https://doi.org/10.1016/j.joule.2020.12.020.
- (15) Rangarajan, S. P.; Barsukov, Y.; Mukherjee, P. P. In Operando Signature and Quantification of Lithium Plating. *J Mater Chem A Mater* **2019**, 7 (36), 20683–20695. https://doi.org/10.1039/c9ta07314k.
- (16) Fear, C.; Adhikary, T.; Carter, R.; Mistry, A. N.; Love, C. T.; Mukherjee, P. P. In Operando Detection of the Onset and Mapping of Lithium Plating Regimes during Fast Charging of Lithium-Ion Batteries. *ACS Appl Mater Interfaces* **2020**, *12* (27), 30438–30448. https://doi.org/10.1021/acsami.0c07803.
- (17) Bloom, I.; Jansen, A. N.; Abraham, D. P.; Knuth, J.; Jones, S. A.; Battaglia, V. S.; Henriksen, G. L. Differential Voltage Analyses of High-Power, Lithium-Ion Cells 1. Technique and Application. *J Power Sources* **2005**, *139* (1–2), 295–303. https://doi.org/10.1016/j.jpowsour.2004.07.021.
- (18) Dubarry, M.; Liaw, B. Y. Identify Capacity Fading Mechanism in a Commercial LiFePO4 Cell. J Power Sources 2009, 194 (1), 541–549. https://doi.org/10.1016/j.jpowsour.2009.05.036.
- (19) Chen, Y.; Torres-castro, L.; Chen, K.; Penley, D.; Lamb, J.; Karulkar, M.; Dasgupta, N. P. Operando Detection of Li Plating during Fast Charging of Li-Ion Batteries Using Incremental Capacity Analysis. *J Power Sources* **2022**, *539* (April), 231601. https://doi.org/10.1016/j.jpowsour.2022.231601.
- (20) Finegan, D. P.; Quinn, A.; Wragg, D. S.; Colclasure, A. M.; Lu, X.; Tan, C.; Heenan, T. M. M.; Jervis, R.; Brett, D. J. L.; Das, S.; Gao, T.; Cogswell, D. A.; Bazant, M. Z.; di Michiel, M.; Checchia, S.; Shearing, P. R.; Smith, K. Spatial Dynamics of Lithiation and Lithium Plating during High-Rate Operation of Graphite Electrodes. *Energy Environ Sci* **2020**, *13* (8), 2570–2584. https://doi.org/10.1039/d0ee01191f.
- (21) Paul, P. P.; Thampy, V.; Cao, C.; Steinrück, H. G.; Tanim, T. R.; Dunlop, A. R.; Dufek, E. J.; Trask, S. E.; Jansen, A. N.; Toney, M. F.; Nelson Weker, J. Quantification of Heterogeneous, Irreversible Lithium Plating in Extreme Fast Charging of Lithium-Ion Batteries. *Energy Environ Sci* **2021**, *14* (9), 4979–4988. https://doi.org/10.1039/d1ee01216a.
- (22) Tanim, T. R.; Paul, P. P.; Thampy, V.; Cao, C.; Steinrück, H. G.; Nelson Weker, J.; Toney, M. F.; Dufek, E. J.; Evans, M. C.; Jansen, A. N.; Polzin, B. J.; Dunlop, A. R.; Trask, S. E. Heterogeneous Behavior of Lithium Plating during Extreme Fast Charging. *Cell Rep Phys Sci* **2020**, *1* (7). https://doi.org/10.1016/j.xcrp.2020.100114.
- (23) Sun, F.; He, X.; Jiang, X.; Osenberg, M.; Li, J.; Zhou, D.; Dong, K.; Hilger, A.; Zhu, X.; Gao, R.; Liu, X.; Huang, K.; de Ning; Markötter, H.; Zhang, L.; Wilde, F.; Cao, Y.; Winter, M.; Manke, I. Advancing Knowledge of Electrochemically Generated Lithium Microstructure and Performance Decay of Lithium Ion Battery by Synchrotron X-Ray Tomography. *Materials Today* **2019**, *27* (August), 21–32. https://doi.org/10.1016/j.mattod.2018.11.003.
- (24) Wandt, J.; Jakes, P.; Granwehr, J.; Eichel, R. A.; Gasteiger, H. A. Quantitative and Time-Resolved Detection of Lithium Plating on Graphite Anodes in Lithium Ion Batteries. *Materials*

- *Today* **2018**, *21* (3), 231–240. https://doi.org/10.1016/j.mattod.2017.11.001.
- (25) Zinth, V.; Lüders, C. von; Hofmann, M.; Hattendorff, J.; Buchberger, I.; Erhard, S.; Rebelo-kornmeier, J.; Jossen, A.; Gilles, R. Lithium Plating in Lithium-Ion Batteries at Sub-Ambient Temperatures Investigated by in Situ Neutron Diffraction. *J Power Sources* **2014**, *271*, 152–159. https://doi.org/10.1016/j.jpowsour.2014.07.168.
- von Lüders, C.; Zinth, V.; Erhard, S. v.; Osswald, P. J.; Hofmann, M.; Gilles, R.; Jossen, A. Lithium Plating in Lithium-Ion Batteries Investigated by Voltage Relaxation and in Situ Neutron Diffraction. *J Power Sources* **2017**, *342*, 17–23. https://doi.org/10.1016/j.jpowsour.2016.12.032.
- (27) Cheng, Q.; Wei, L.; Liu, Z.; Ni, N.; Sang, Z.; Zhu, B.; Xu, W.; Chen, M.; Miao, Y.; Chen, L. Q.; Min, W.; Yang, Y. Operando and Three-Dimensional Visualization of Anion Depletion and Lithium Growth by Stimulated Raman Scattering Microscopy. *Nat Commun* **2018**, *9* (1). https://doi.org/10.1038/s41467-018-05289-z.
- (28) Cheng, Q.; Jin, T.; Miao, Y.; Liu, Z.; Borovilas, J.; Zhang, H.; Liu, S.; Kim, S.-Y.; Zhang, R.; Wang, H.; Chen, X.; Chen, L.-Q.; Li, J.; Min, W.; Yang, Y. Stabilizing Lithium Plating in Polymer Electrolytes by Concentration-Polarization-Induced Phase Transformation. *Joule* **2022**, 6 (10), 2372–2389.
- (29) Guo, Z.; Zhu, J.; Feng, J.; Du, S. Direct in Situ Observation and Explanation of Lithium Dendrite of Commercial Graphite Electrodes. *RSC Adv* **2015**, *5* (85), 69514–69521. https://doi.org/10.1039/c5ra13289d.
- (30) Harris, S. J.; Timmons, A.; Baker, D. R.; Monroe, C. Direct in Situ Measurements of Li Transport in Li-Ion Battery Negative Electrodes. *Chem Phys Lett* **2010**, *485* (4–6), 265–274. https://doi.org/10.1016/j.cplett.2009.12.033.
- (31) Agrawal, S.; Bai, P. Operando Electrochemical Kinetics in Particulate Porous Electrodes by Quantifying the Mesoscale Spatiotemporal Heterogeneities. *Adv Energy Mater* **2021**, *11* (12). https://doi.org/10.1002/aenm.202003344.
- (32) Agrawal, S.; Bai, P. Dynamic Interplay between Phase Transformation Instabilities and Reaction Heterogeneities in Particulate Intercalation Electrodes. *Cell Rep Phys Sci* **2022**, *3* (5), 100854. https://doi.org/10.1016/j.xcrp.2022.100854.
- (33) Bai, P.; Li, J.; Brushett, F. R.; Bazant, M. Z. Transition of Lithium Growth Mechanisms in Liquid Electrolytes. *Energy Environ Sci* **2016**, *9* (10), 3221–3229. https://doi.org/10.1039/c6ee01674j.
- (34) Lee, Y.; Ma, B.; Bai, P. Concentration Polarization and Metal Dendrite Initiation in Isolated Electrolyte Microchannels. *Energy Environ Sci* **2020**, 3504–3513. https://doi.org/10.1039/d0ee01874k.
- (35) Ma, B.; Lee, Y.; Bai, P. Dynamic Interfacial Stability Confirmed by Microscopic Optical Operando Experiments Enables High-Retention-Rate Anode-Free Na Metal Full Cells. *Advanced Science* **2021**, *8* (12), 1–11. https://doi.org/10.1002/advs.202005006.
- (36) Ma, B.; Bai, P. Fast Charging Limits of Ideally Stable Metal Anodes in Liquid Electrolytes. *Adv Energy Mater* **2022**, *2102967*, 1–9. https://doi.org/10.1002/aenm.202102967.
- (37) Ma, B.; Sittisomwong, P.; Ma, J.; Bai, P. Effects of Interfacial Solvation Structures on the Morphological Stability of Potassium Metal Anodes Revealed by Operando Diagnosis . *ACS Appl Energy Mater* **2022**. https://doi.org/10.1021/acsaem.2c00716.

- (38) Smith, R. B.; Khoo, E.; Bazant, M. Z. Intercalation Kinetics in Multiphase-Layered Materials. *Journal of Physical Chemistry C* **2017**, *121* (23). https://doi.org/10.1021/acs.jpcc.7b00185.
- (39) Bazant, M. Z. Theory of Chemical Kinetics and Charge Transfer Based on Nonequilibrium Thermodynamics. *Acc Chem Res* **2013**, *46* (5). https://doi.org/10.1021/ar300145c.
- (40) Abe, Y.; Hori, N.; Kumagai, S. Electrochemical Impedance Spectroscopy on the Performance Degradation of LiFePO4/Graphite Lithium-Ion Battery Due to Charge-Discharge Cycling under Different c-Rates. *Energies (Basel)* **2019**, *12* (23), 1–14. https://doi.org/10.3390/en12234507.
- (41) Levi, M. D.; Aurbach, D. The Application of Electroanalytical Methods to the Analysis of Phase Transitions during Intercalation of Ions into Electrodes. In *Journal of Solid State Electrochemistry*; 2007; Vol. 11. https://doi.org/10.1007/s10008-007-0264-x.
- (42) Smith, R. B.; Bazant, M. Z. Multiphase Porous Electrode Theory. *J Electrochem Soc* **2017**, *164* (11). https://doi.org/10.1149/2.0171711jes.
- (43) Newman, J.; Thomas-Alyea, K. Electrochemical Systems, 3rd ed.; Wiley: New York, 2004.
- (44) Mu, G.; Agrawal, S.; Sittisomwong, P.; Bai, P. Impacts of Negative to Positive Capacities Ratios on the Performance of Next-Generation Lithium-Ion Batteries. *Electrochim Acta* **2022**, *406*. https://doi.org/10.1016/j.electacta.2022.139878.
- (45) Li, T.; Yuan, X. Z.; Zhang, L.; Song, D.; Shi, K.; Bock, C. Degradation Mechanisms and Mitigation Strategies of Nickel-Rich NMC-Based Lithium-Ion Batteries. *Electrochemical Energy Reviews*. 2020. https://doi.org/10.1007/s41918-019-00053-3.
- (46) Li, Q.; Jiao, S.; Luo, L.; Ding, M. S.; Zheng, J.; Cartmell, S. S.; Wang, C. M.; Xu, K.; Zhang, J. G.; Xu, W. Wide-Temperature Electrolytes for Lithium-Ion Batteries. ACS Appl Mater Interfaces 2017, 9 (22), 18826–18835. https://doi.org/10.1021/acsami.7b04099.
- (47) Anseán, D.; Baure, G.; González, M.; Cameán, I.; García, A. B.; Dubarry, M. Mechanistic Investigation of Silicon-Graphite/LiNi0.8Mn0.1Co0.1O2 Commercial Cells for Non-Intrusive Diagnosis and Prognosis. *J Power Sources* **2020**, *459*. https://doi.org/10.1016/j.jpowsour.2020.227882.

Table of Contents

